JOURNAL OF AIRCRAFT
Vol. 43, No. 2, March–April 2006

Two-Dimensional Simulation of Dynamic Surface Roughness for Aerodynamic Flow Control

W. W. Huebsch*
West Virginia University, Morgantown, West Virginia 26506-6106

This study addresses the issue of controlling flow separation through the use of dynamic surface roughness. The work focuses on two areas: 1) development of simulation tools for detailed analysis of moving flow boundaries and 2) investigation of the effects of dynamic roughness on aerodynamic flow separation. The process of generating a quality grid for a surface that contains complex roughness can be a labor-intensive project. The addition of dynamic surface roughness, or roughness that grows (or shrinks) in time, can further complicate this process. The current study proposes a method that not only accounts for the perturbations to the surface but also allows for the surface to move dynamically, which produces a robust gridding method that is well suited for this application. The method is applied to dynamic surface roughness in the leading-edge region of an airfoil but could also be used for analysis of internal surface roughness. The dynamic surface roughness examined in this study demonstrated a major effect on the flow field, with the resulting flow being significantly different than the flow found with similar static surface roughness. The dynamic roughness was able to delay or eliminate the unsteady flow separation for the conditions tested at both constant angle of attack and dynamic stall regimes and shows strong potential as an aerodynamic-flow-control mechanism.

Nomenclature

A	=	maximum roughness height
F	=	frequency of dynamic roughness
$f(\xi, \tau)$	=	analytic expression for roughness geometry
g	=	scale factor
$h(\tau)$	=	time-dependent hump height
$K(t)$	=	angle-of-attack parameter
l	=	leading-edge radius of curvature for parabola
Sr	=	Strouhal number
$\eta', \eta, \bar{\eta}$	=	normal coordinates
λ	=	wavelength for single roughness element
$\xi', \xi, \bar{\xi}$	=	streamwise coordinates
τ', τ, t	=	temporal terms
Ψ, ψ	=	stream function
Ω, ω	=	vorticity

Subscripts

inv	=	inviscid value
L, R	=	left and right locations, respectively
PT	=	pseudo time
w	=	value at the wall
∞	=	freestream value

I. Introduction

AS the area of computational fluid dynamics (CFD) has progressed over the years, researchers continually increase the complexity of problems that can be solved, both in the problem formulation and the physics. This study investigates surface-roughness effects on the flow field and the effect on this flow field if the roughness is allowed to move dynamically. A time-dependent roughness (i.e., dynamic roughness) placed on an aerodynamic surface has the potential for boundary-layer flow control in general; this work is limited to control of flow separation, which is a common hindrance in aerodynamic flows. This type of problem requires a moving boundary, which is often termed a Stefan problem.[1] The current work focuses on two areas: 1) development of simulation tools for detailed analysis of moving flow boundaries and 2) preliminary investigation of the effects of dynamic roughness on aerodynamic flow separation.

There has been work done in the past on both the numerical aspects of integrating a moving boundary into the numerical flow simulation and the effect of a moving boundary on the flow field. Many of the most popular numerical methods and techniques have been compiled by authors such as Zerroukat and Chatwin[2] as well as Shyy et al.[3] One technique that Shyy et al. discuss that is relevant to the current work is the transformation methods with body-fitted coordinates. Crank[1] lists this technique as a "front-fixing" method, where the boundary can be fixed by the choice of a new or updated space coordinate. A transformation is used to map an irregular shape into a fixed rectangular domain in computational space. If the boundary is moving with time, such as dynamic roughness, the physical boundary changes with time but the mapped computational domain is fixed for all time. However, this method is prone to difficulties if the surface perturbation, whether static or dynamic, becomes multivalued or folds back on itself. The required transformations for this method do increase the complexity of the derivation, but as the next section shows, this is a one-time expense. The resulting algorithm tends to be robust and capable of dealing with a wide variety of surface perturbations.

There has been some experimental, theoretical, and numerical work done in the past on the effect of a moving boundary on the accompanying flow field. Some examples of flow-control efforts[4] include the use of riblets, laminar flow control with boundary-layer blowing, suction or wall cooling, and bubble injection and polymer addition for turbulent boundary layers. There has been research in both internal and external flow applications. Pedley and Stephanoff[5] conducted experiments for channel flow with one wall having a time-dependent indentation. This work showed that, depending on the Reynolds and Strouhal numbers, a wavetrain was formed downstream of the cycling indentation and eddies were formed in the separated flow region, which were convected downstream. Chauve and Schiestel[6] also performed experiments, as well as numerical simulations, of turbulent pipe flow with periodic small-amplitude wall undulations (or time-dependent indentations). Their work revealed that the resulting flow was quite different from that of a static pipe wall. Although the amplitude of the wall undulations was quite

Presented as Paper 2004-587 at the AIAA 42nd Aerospace Sciences Meeting, Reno, NV, 5–8 January 2004; received 23 November 2004; revision received 10 May 2005; accepted for publication 12 May 2005.

*Assistant Professor, P.O. Box 6106, Mechanical and Aerospace Engineering. Member AIAA.

small, their work revealed the existence of an unsteady reverse-flow region downstream of each crest. Both of these studies focused on internal flows, but the type of moving boundary that was used has ties with the dynamic roughness investigated in this work. It should be noted that this type of internal flow with a moving boundary is starting to find some application in bioengineering (such as modeling flow through arteries or the respiratory tract). With respect to the current research area, wall oscillations (e.g., Lekoudis and Sengupta[7]) and compliant surfaces (e.g., Bushnell et al.[8]) have also been investigated as a means of flow control and skin-friction drag reduction.

There is also work relating moving boundaries to external flow applications. The work by Duck[9,10] in part investigates external incompressible flow past an unsteady wall distortion through the use of triple-deck theory. Results from this work show that the disturbances from the unsteady perturbation tend to grow as they move downstream as a result of triggering the Tollmien-Schlichting (TS) instability. Rediniotis et al.[11] have conducted preliminary work in the use of an active "smart" skin for turbulent drag reduction in aerodynamic flows. The skin is actively deformed to mimic a traveling wave, which is based on evidence that shows transverse traveling waves with specific characteristics can result in turbulent drag reduction. This indicates that the character of the dynamic motion of the roughness may be an important parameter in flow control. Folk and Ho[12] used micro-electro-mechanical systems (MEMS) to activate microbubbles on the surface of a delta wing. The surface perturbations alter the global vortex pair and are used as a method of maneuvering the aircraft. Small-scale devices are able to create large global changes in the vortex system because flow separation is extremely sensitive to perturbations at the separation point or separation line. This work most closely matches the dynamic roughness mechanism described in the present work.

Greenblatt and Wygnanski[13] provide a review of the control of flow separation from aerodynamic surfaces through periodic excitation. The dynamic roughness applied in this study could fall under the umbrella of periodic excitation. Much of the work reviewed focuses on oscillatory blowing to achieve the periodic excitation. There has been a fair amount of successful work in this area that has produced a methodology for control of flow separation and an increase in C_L values for airfoils and wings. One key finding is that the entrainment of the boundary layer can be significantly altered by small amplitude excitation. Whether the mechanism is oscillatory blowing, vibrating ribbons, or piezoelectric-based diaphragms, the result is an oscillatory addition of momentum to the fluid, which can affect flow separation.

The author defines dynamic roughness as small time-dependent perturbations to the airfoil or wing surface as a potential mechanism for controlling flow separation. In the most basic form, there would be humps placed in the leading-edge region of the wing that would have the ability to expand and contract at a specific frequency and reach a maximum height such that flow separation would be delayed or eliminated for a certain flight condition. An example of a dynamic roughness configuration is depicted in Fig. 1. This figure depicts three-dimensional roughness elements on the surface, although the simulations and roughness geometries in this study are two-dimensional in nature. Clearly the resulting flow field will be different with the two-dimensional and three-dimensional dynamic roughness, but the two-dimensional simulations are used for a preliminary investigation into the flow control mechanisms. However, it should also be noted that dynamic roughness could take the form of two-dimensional spanwise strips on a three-dimensional wing. Future research directions will include three-dimensional dynamic roughness.

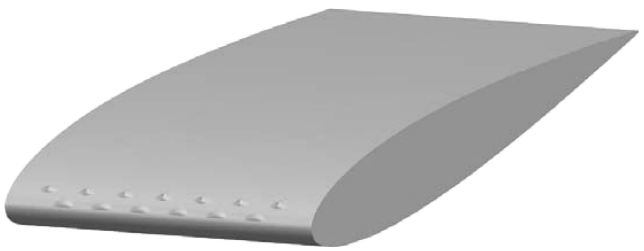

Fig. 1 Example of dynamic roughness on an aerodynamic surface, fully expanded.

In general, the goals of flow control are an increase in performance and a reduction in drag. A primary objective associated with these goals is the delay or elimination of flow separation from an aerodynamic surface, which directly relates to the current study. Other objectives include the delay of boundary-layer transition or reducing skin-friction drag once the boundary layer is fully turbulent. The research study described here uses dynamic roughness as a mechanism to control flow separation from an aerodynamic surface. The primary focus is flow separation, although this technique may also have application to the delay of boundary-layer transition or reduction of turbulent skin-friction drag. White and Saric[14] found that three-dimensional static roughness could be an effective tool in delaying transition to turbulence and also indicated that transition delay would be feasible through a type of dynamic roughness. Therefore, it is likely that the dynamic roughness used to affect flow separation in this study could also be used to affect boundary-layer transition, at least for certain areas of parameter space.

The current method combines the body-fitted grid technique with the shearing transformation, or Prandtl transposition (as outlined in subsequent sections), to accommodate the time-dependent surface perturbations. There are obvious advantages in using a finite-difference scheme with discrete grid points on the moving boundary in conjunction with body-fitted coordinates, as opposed to some type of interpolation of the grid to the surface.

The actual dynamic motion of the solid boundary usually falls into two categories: the time-dependent motion is either known a priori or is unknown and has to be determined as part solution. For applications such as fluid–structure interaction, the moving boundary is coupled to the governing flow equations and must be solved as part of the system. For this preliminary work, the dynamic motion of the boundary is prescribed. For the applications envisioned for the current algorithm, the movement of the boundary will generally be either known or the timescale will be large enough that the moving boundary will be quasi steady. However, the method described in the next section could be adapted to a situation where the boundary location is an unknown quantity of the solution. The dynamic roughness can take many forms with variations in chord location, maximum height of expansion, frequency of expansion/contraction, number of roughness elements, configuration of roughness layout, and characterization of the roughness motion. It is expected that there will be optimal settings of dynamic roughness parameters given a specific set of flight conditions, including Reynolds number and angle of attack.

In the present work, an algorithm has been adapted to study the effect of dynamic surface roughness on the external flow field. The roughness shapes are located in the leading-edge region of an airfoil. This flow solver uses the full Navier–Stokes equations with fine grid resolution capable of capturing small-scale flow structures within the boundary layer but in a two-dimensional space. Several unique items are employed in this work to augment the study of dynamic roughness. The two-dimensional algorithm focuses resources on the leading-edge region of an airfoil where initial flow separation can be affected and where aerodynamic phenomena are critical, such as the suction peak. This is accomplished by solving the flow field around a semi-infinite parabola, which can be used to simulate the leading-edge region of the NACA 00XX series airfoils, and properly treating the downstream flow. Solving the flow around the leading edge and not including the entire airfoil allows the use of a large number of grid points in the area of interest. A dense grid is placed in the leading-edge region that encompasses the dynamic surface roughness and downstream of the roughness.

Under certain conditions, the dynamic roughness will produce a significant change in the downstream flow as compared to static roughness with comparable maximum height. Parameters that affect this process include the Reynolds and Strouhal numbers, the relative roughness height with respect to the boundary layer, geometric

roughness configurations, and roughness placement. Moreover, the configuration of the airfoil with respect to the freestream will also affect the results; whether the airfoil is aligned with the flow or at angle of attack, and whether the airfoil is undergoing a dynamic process such as rapid pitchup (i.e., dynamic stall scenario).

One potential advantage of the dynamic roughness as a flow control device may be power savings. Traditional boundary-layer control has included such popular methods as either blowing or suction. Greenblatt and Wygnanski[13] point out that the two main drawbacks for this methodology are 1) complex and heavy plumbing systems and 2) excessive power requirements from auxiliary compressors. Dynamic roughness has the potential to overcome both of these drawbacks. The power required to activate the dynamic roughness should be reduced by using small electromechanical devices to perturb the surface of the skin. With the current state of the art in actuator design and flexible skin, dynamic roughness is feasible for aerodynamic flow control. Passive flow control devices such as vortex generators do not have the added power requirements but often have some consistent added penalty because of added drag, whereas the dynamic roughness can be employed only when needed.

II. Flow Analysis

This section outlines the governing equations used for the flow calculations, the corresponding boundary conditions, and the roughness geometry parameters. In addition, a brief section is included on the numerical method employed for these simulations. For brevity, only the key elements of these items are discussed. A more thorough description is provided by Huebsch and Rothmayer.[15]

A. Governing Flow Equations

The flow is modeled by the full Navier–Stokes equations for two-dimensional, unsteady, incompressible flow. The x and y coordinates are nondimensionalized by the leading-edge radius of curvature l, the u and v velocities by the free-stream velocity V_∞, and the time t by l/V_∞. The resulting dimensionless Navier–Stokes equations cast in the Cartesian coordinate system and written in stream function-vorticity form are given as follows:

$$\psi_{xx} + \psi_{yy} = -\omega \tag{1}$$

$$\omega_t + \psi_y \omega_x - \psi_x \omega_y = Re^{-1}(\omega_{xx} + \omega_{yy}) \tag{2}$$

where ψ and ω are the two-dimensional stream function and vorticity, respectively.

The leading edge of the airfoil is approximated by using a semi-infinite parabola, in a manner similar to work by Werle and Davis.[16] The results for flow past a parabola compare well with computational results for the NACA 0012 airfoil[17] and may be used to simulate any of the NACA 00XX series with different thicknesses because the leading edges of these airfoils are nearly parabolic in shape. The parabola matches the airfoil leading edge up to approximately 6% of chord.

The stream-function and vorticity-transport equations [Eqs. (1) and (2)] are taken through multiple transformations to arrive at the final governing equations. These transformations are performed for several reasons: 1) to produce an orthogonal body-fitted grid, 2) to account for the surface roughness within the governing equations, and 3) to implement stretching and clustering of the grid lines for flow resolution. The first transformation uses conformal mapping to cast the governing equations in a parabolic coordinate system, which produces a body-fitted grid. Use of the body-fitted coordinates in a moving grid application with transformed governing equations is similar to the work of Shyy et al.[18] The parabolic coordinate system is related to the Cartesian system through the following transformations:

$$x = \left(\xi'^2 - \eta'^2\right)/2, \qquad y = \xi'\eta', \qquad t = \tau' \tag{3}$$

The various coordinate systems and the corresponding nomenclature are shown in Fig. 2.

The surface roughness is introduced through the use of a Prandtl transposition (or shearing transformation) similar to the work of

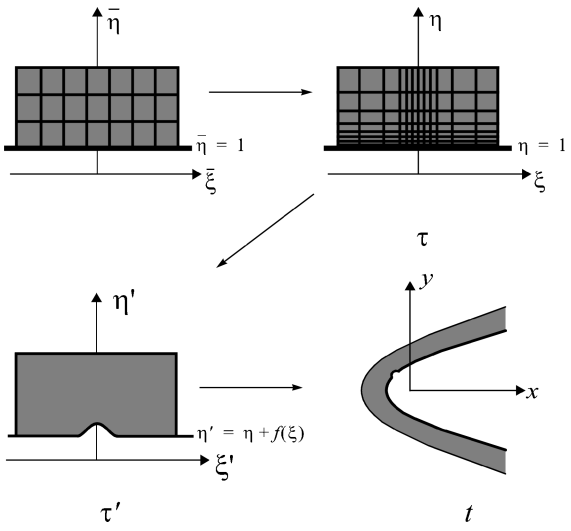

Fig. 2 Schematic diagram of the overall transformation from the computational space to physical space.

Huebsch and Rothmayer.[15] Applying this transformation allows the surface perturbations to be directly embedded within the governing equations. This also allows straightforward inclusion of a moving boundary capability. This technique can be used on a wide range of roughness shapes (from simple to complex). To include the static or dynamic surface roughness, the following transformations are applied to the governing equations:

$$\xi' = \xi, \qquad \eta' = \eta + f(\xi, \tau), \qquad \tau' = \tau \tag{4}$$

The conversion from τ' to τ yields the following chain-rule expression:

$$\frac{\partial}{\partial \tau'} = \underline{\eta_{\tau'} \frac{\partial}{\partial \eta}} + \frac{\partial}{\partial \tau} \tag{5}$$

The underlined term in Eq. (5) accounts for the moving surface. If the surface is static, this term goes to zero. In the present derivation, the time dependency is only in the normal direction; that is, the dynamic roughness is only changing in the η direction, whereas the ξ direction is static. If the surface perturbation was dynamic in both the streamwise and normal directions, the same methodology would still apply.

The surface roughness is added to the baseline parabolic surface through the Prandtl transposition, which allows new surface-oriented coordinates to be easily generated without the need for regridding; therefore, alterations to the surface-roughness geometry can be made without changing the actual grid parameters. The current work uses an analytic expression to describe the roughness geometry. Both simple and complex roughness can be defined in this fashion. The roughness equation used is as follows:

$$f(\xi, \tau) = h(\tau)(\xi - \xi_L)^5(\xi_R - \xi)^5 \tag{6}$$

where h is the time-dependent hump height and ξ_L, ξ_R are the left and right endpoints of the hump, respectively. Similar to a quartic hump, a 10th-order polynomial was used to ensure a smooth transition from the roughness element to the baseline surface. This helped to alleviate any curvature discontinuity problems at the juncture point. Because the roughness geometry is embedded in the governing equations, including the second derivative, the algorithm is sensitive to a discontinuity even in the second derivative.

The $h(\tau)$ term in Eq. (6) dictates that the dynamic roughness is only varying in the normal direction, which is the time-dependent change in height of the roughness. If the roughness is static, then the derivative of f with respect to τ would go to zero and the additional term in the vorticity transport equation would go to zero. The preliminary method of describing the dynamic height of the

roughness is given as

$$h(\tau) = A|\sin(2\pi\tau/\lambda)| \tag{7}$$

where A is the maximum height of the roughness. The dynamic motion of the roughness follows a sinusoidal pattern, which is constrained as an absolute value so that the roughness is either a positive perturbation to the surface or flush with the surface. If static roughness is desired, the algorithm automatically sets $h(\tau)$ equal to A to establish the roughness height.

The dynamic roughness can take the shape of either simple or complex surface roughness. The simple roughness is either a single hump or multiple humps with equal height and wavelength arranged to simulate distributed roughness. The complex roughness is created by superimposing multiple humps of varying heights and wavelengths to produce a more geometrically complex shape (although only the normal direction is time dependent at this time).

The final transformation helps to resolve the flow in the vicinity of the roughness and near the surface with grid stretching and grid clustering given by the generic terms $\bar{\xi} = \bar{\xi}(\xi)$, $\bar{\eta} = \bar{\eta}(\eta)$. The overall transformation from the uniform-grid computational space to physical space is summarized in Fig. 2.

After these transformations, the final stream-function and vorticity-transport equations have the following form:

$$\bar{\xi}_{\xi\xi}\Psi_{\bar{\xi}} + (\bar{\xi}_{\xi})^2\Psi_{\bar{\xi}\bar{\xi}} - f_{\xi\xi}\bar{\eta}_{\eta}\Psi_{\bar{\eta}} - 2f_{\xi}\bar{\xi}_{\xi}\bar{\eta}_{\eta}\Psi_{\bar{\xi}\bar{\eta}} + \left[1 + (f_{\xi})^2\right]\bar{\eta}_{\eta\eta}\Psi_{\bar{\eta}} + \left[1 + (f_{\xi})^2\right](\bar{\eta}_{\eta})^2\Psi_{\bar{\eta}\bar{\eta}} = (-g^2)\Omega + \Psi_{\mathrm{pt}} \tag{8}$$

and

$$\Omega_{\mathrm{pt}} + g^2[\underline{(-f_{\tau})\bar{\eta}_{\eta}\Omega_{\bar{\eta}}} + \Omega_{\tau}] + \bar{\xi}_{\xi}\bar{\eta}_{\eta}(\Psi_{\bar{\eta}}\Omega_{\bar{\xi}} - \Psi_{\bar{\xi}}\Omega_{\bar{\eta}}) + (\psi_{\mathrm{inv}})_{\eta}\bar{\xi}_{\xi}\Omega_{\bar{\xi}} - f_{\xi}(\psi_{\mathrm{inv}})_{\eta}\bar{\eta}_{\eta}\Omega_{\bar{\eta}} - (\psi_{\mathrm{inv}})_{\xi}\bar{\eta}_{\eta}\Omega_{\bar{\eta}} = Re^{-1}\left\{\bar{\xi}_{\xi\xi}\Omega_{\bar{\xi}} + (\bar{\xi}_{\xi})^2\Omega_{\bar{\xi}\bar{\xi}} - f_{\xi\xi}\bar{\eta}_{\eta}\Omega_{\bar{\eta}} - 2f_{\xi}\bar{\xi}_{\xi}\bar{\eta}_{\eta}\Omega_{\bar{\xi}\bar{\eta}} + \left[1 + (f_{\xi})^2\right]\bar{\eta}_{\eta\eta}\Omega_{\bar{\eta}} + \left[1 + (f_{\xi})^2\right](\bar{\eta}_{\eta})^2\Omega_{\bar{\eta}\bar{\eta}}\right\} \tag{9}$$

where $g^2 = \xi^2 + \eta^2 + 2\eta f + f^2$. The f term represents the roughness geometry and is a function of (ξ, τ). It should be noted that this term along with its derivatives (f_{ξ}, $f_{\xi\xi}$, f_{τ}) are contained within the governing equations. The underlined termed in the vorticity transport equation [Eq. (9)] is generated from time-dependent roughness growth through the Prandtl transposition. If the roughness was static, this term would go to zero. Gad-el-Hak[19] notes that the wall motion can establish the surface as a source of vorticity. These alterations control the instantaneous and mean velocity profiles at the wall, which affect such things as wall skin friction and the ability of the boundary layer to resist separation. The underlined term indicates injection of vorticity normal to the surface into the boundary-layer region.

To aid in the convergence of the algorithm, the stream function and vorticity terms are split into inviscid (ψ_{inv}) and viscous (Ψ, Ω) components. To help stabilize the method during global iterations, a fictitious time-derivative term (or pseudo-time term) is added to both the stream-function Poisson equation and the vorticity-transport equation (i.e., Ψ_{pt} and Ω_{pt}, respectively). At each physical time step, the solution is converged in pseudo time.

B. Inviscid Flow

An analytic solution for the inviscid potential flow past a clean parabola was given by Van Dyke.[20] Applying the Prandtl transposition to this equation produces the inviscid potential solution for the stream function with surface roughness present:

$$\psi_{\mathrm{inv}} = (\xi + K)(\eta + f(\xi, \tau) - 1) \tag{10}$$

where K is the vertical displacement of the stagnation point from the vertex of the parabola and is termed the angle-of-attack parameter. K can be related to the angle of attack of the airfoil when the parabolic leading edge is coupled to a thin airfoil description of the full airfoil. In the present study, K is an input parameter that is either constant or a known function of time. $K(t)$ can be used to simulate any desired motion of the parabola relative to the freestream (i.e., the parabola remains fixed as the stagnation point traverses the leading edge).

C. Boundary Conditions

No-slip boundary conditions, with $u = v = 0$, are applied at the surface of the parabola. In terms of the stream function, this boundary condition is $\psi = 0$ and $\psi_{\eta} = 0$. Applying the flow-variable splitting, these boundary conditions become

$$\Psi = -\psi_{\mathrm{inv}} \qquad \text{and} \qquad \Psi_{\bar{\eta}} = -(\psi_{\mathrm{inv}})_{\eta}/\bar{\eta}_{\eta} \quad \text{at} \quad \eta = 1 \tag{11}$$

A second-order-accurate one-sided finite-difference formulation is used for the derivative in this equation.

At the far-field boundary, η large but finite, the viscous effects die out and a fully inviscid flow is recovered. Therefore, the split viscous variables Ψ and Ω are assumed to be zero at this boundary. The viscous solution for flow past a parabola is known to approach the Blasius solution as $\xi \to \infty$ (Davis[21]). The upper and lower downstream boundaries are placed at a large but finite values of $|\xi|$.

D. Numerical Method

An implicit numerical method is used to solve the governing flow equations. The numerical scheme is second-order accurate in time and space, with central differences used for the spatial derivatives and a backward difference for the temporal derivative. The nonlinear convective terms are linearized using Newton linearization, whereas mixed-derivatives are treated iteratively as source terms.

The implicit scheme sweeps in both the ξ and η directions, with the sweeps in the ξ direction being bidirectional and the sweeps in η being unidirectional. One complete spatial sweep consists of two alternating sweeps in the streamwise direction (ξ) and one sweep in the normal direction (η), which is equivalent to one pseudo time step. Each sweep involves the solution of a 2×2 block-tridiagonal system of equations.

For unsteady flow, the code marches the solution in time, and at each physical time step, the pseudo time terms are iterated to convergence before moving to the next physical time step. The algorithm has the capability of solving for purely steady flow by either 1) allowing the unsteady code to eventually converge to a steady solution or 2) eliminating the time term, Ω_{τ}, and solving the remaining steady Navier–Stokes equations. With this particular algorithm, if the flow field is truly steady, then either method can be used to obtain the solution. If the flow is unsteady, then the "steady" flow solver may not converge.

The grid used for the computations is a structured, body-fitted grid. A region of dense, uniformly spaced grid points in the streamwise direction is placed in the vicinity of the surface roughness, with hyperbolic stretching upstream and downstream of this region. Stretching is also used in the normal direction to cluster points near the surface. A typical parabolic grid is shown in Fig. 3. This grid is 481×81, with 381 streamwise grid points placed in the dense-grid region near the leading edge. In this figure, the leading edge of the parabola has a clean surface (i.e., no roughness). When roughness is present, typically the grid requirements are increased to resolve the flow around the complex geometry. The finest grid used is 1501×301, with 1400 grid points clustered in the leading-edge region. Figure 4 shows a typical grid in the vicinity of a single dynamic roughness element that is fully contained within the boundary layer.

III. Results

This work focuses on development of a robust method for incorporating dynamic surface roughness and investigating the effects of time-dependent roughness on the external flow field of an airfoil leading edge. The goal is to demonstrate the potential of dynamic roughness as a flow control mechanism. It is anticipated that this work will stimulate ideas on future investigations of small-scale dynamic roughness to control flow separation. The current algorithm has undergone extensive validation testing for static roughness geometries, which can be found in Refs. 15 and 22.

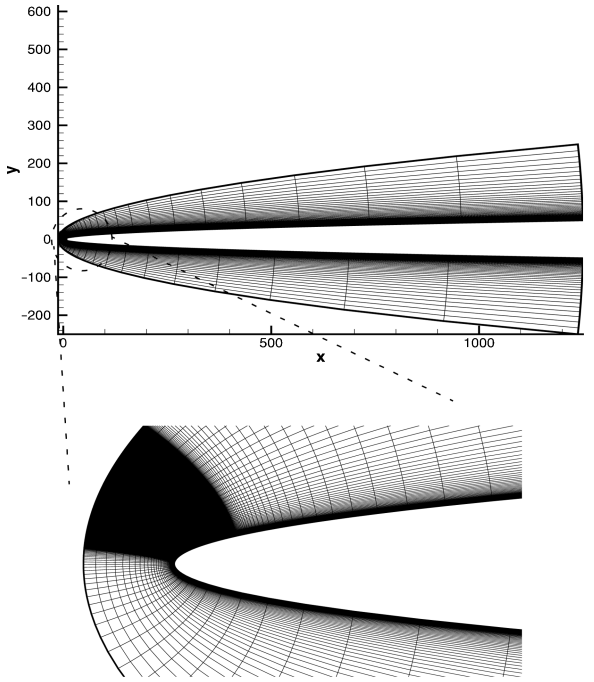

Fig. 3 Typical grid used for flow past the parabola leading edge.

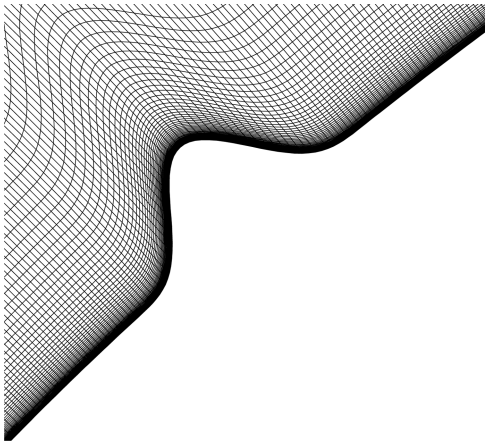

Fig. 4 Body-fitted grid for a simple surface-roughness element.

A. Preliminary Results

The first case that was investigated was a single roughness element placed in the leading-edge region and allowed to expand and contract with time. This dynamic geometry is depicted in Fig. 5. The analytic expression for the hump is given in Eq. (6), and the time dependency is given in Eq. (7). As expected, the frequency of the roughness had to be relatively large to see a change in the flow field between the static and dynamic roughness. Otherwise, the time-dependent roughness appears to be quasi steady with respect to the timescale of the flow.

For a Reynolds number (based on leading-edge radius of curvature) of 1000, the roughness was given an oscillation frequency of 2.0 based on the nondimensional physical time. A time history of the resulting flow is shown in Fig. 6. At $\tau = 0.15$, a visible recirculating region has started to form on the downstream side of the hump. The roughness reaches its maximum height at $\tau = 0.25$, which is approximately the height of the oncoming laminar boundary layer. As the hump is contracting, the separation bubble increases in size at $\tau = 0.35$. The hump is fully retracted (i.e., no roughness) at $\tau = 0.50$ and then begins the cycle again. At this low Reynolds number, the flow remains laminar with no vortex shedding occurring downstream of the roughness. It is expected that the effects of dynamic roughness on the flow field will be dependent upon the Reynolds number.

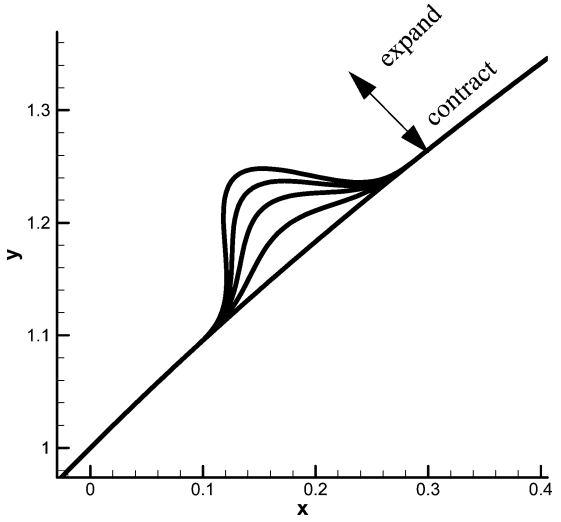

Fig. 5 Dynamic roughness for single-hump geometry.

Figures 7a and 7b show a time history of wall vorticity as a function of streamwise location in the vicinity of a single roughness element during the unsteady expansion and contraction. It should be noted that $-\Omega_w$ is proportional to the wall-shear stress. Figure 7a gives the wall vorticity from $\tau = 0.1$ to $\tau = 0.25$, and Fig. 7b from $\tau = 0.25$ to $\tau = 0.55$. For reference, $\tau = 0.25$ corresponds to the maximum height of the dynamic roughness, whereas $\tau = 0.50$ corresponds to the hump fully contracted. As the hump begins to expand, there is a large increase in wall vorticity, as shown at $\tau = 0.15$. As the hump contracts, the spike in wall vorticity decreases and the values approximately level off at $\tau = 0.50$; the cycle begins again as shown at $\tau = 0.55$. Examining this temporal plot, it can be seen that the dynamic roughness injects a large amount of vorticity into the flow field at the roughness location as demonstrated in Eq. (9). Gad-el-Hak[19] discussed that the wall motion can affect whether the surface is a source or sink of vorticity and at what magnitude, which can ultimately affect the ability of the boundary layer to resist flow separation.

A comparison is made between the flow field past a dynamic roughness element and a static roughness element. The height of the static roughness element is equal to the maximum height achieved by the dynamic roughness. The results are shown in Fig. 8, which reveals significant differences in the two resulting flow fields. For the static roughness (Fig. 8a), a long laminar recirculating region is produced behind the hump and the flow converges to a steady-state solution. For the dynamic roughness (Fig. 8b), the separation bubble is much smaller and hugs the downstream side of the hump. As was shown in Fig. 7, this separation bubble grows in size as the hump starts to contract but still does not reach the streamwise length of the static roughness. Grid studies were performed to ensure that the simulations had the proper grid resolution for the roughness configuration and Reynolds number being tested.

B. Flow Separation at Constant Angle of Attack

With respect to implementing dynamic roughness as a flow control mechanism, two primary cases were investigated: 1) flow separation at a constant angle of attack and 2) flow separation resulting from dynamic stall. This section details the results for the constant angle-of-attack separation.

The angle of attack was chosen such that unsteady flow separation was produced on the upper surface of the leading edge given the Reynolds number. For these cases, the angle-of-attack parameter was set to $K(t) = 2.0$ and the Reynolds number based on leading-edge radius was set to 1000. Using a NACA 0012 for reference, these values would correspond to an angle of attack of 21 deg and a chord Reynolds number of 0.7×10^5, although as a proof of concept for dynamic roughness as a flow control device, physical dimensional numbers associated with actual airfoils are not critical at this point in the study.

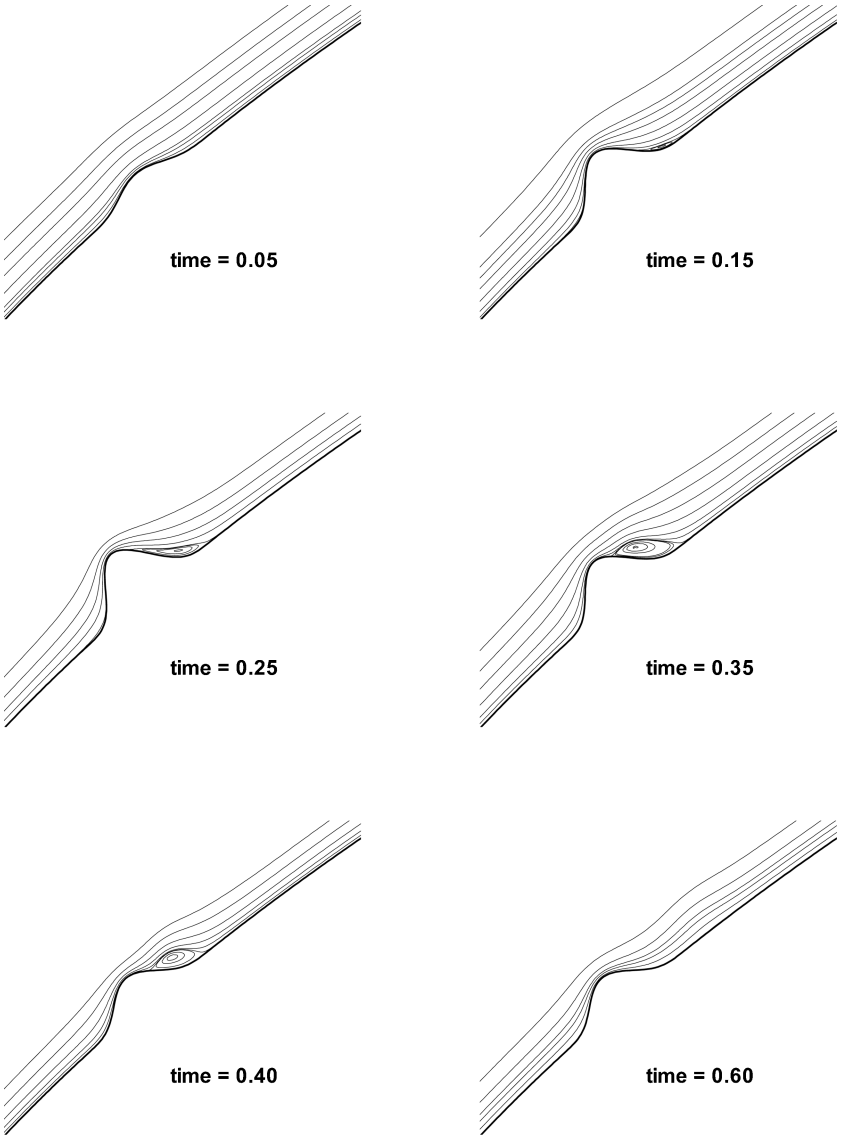

Fig. 6 Unsteady time sequence for the expansion and contraction of the dynamic surface roughness.

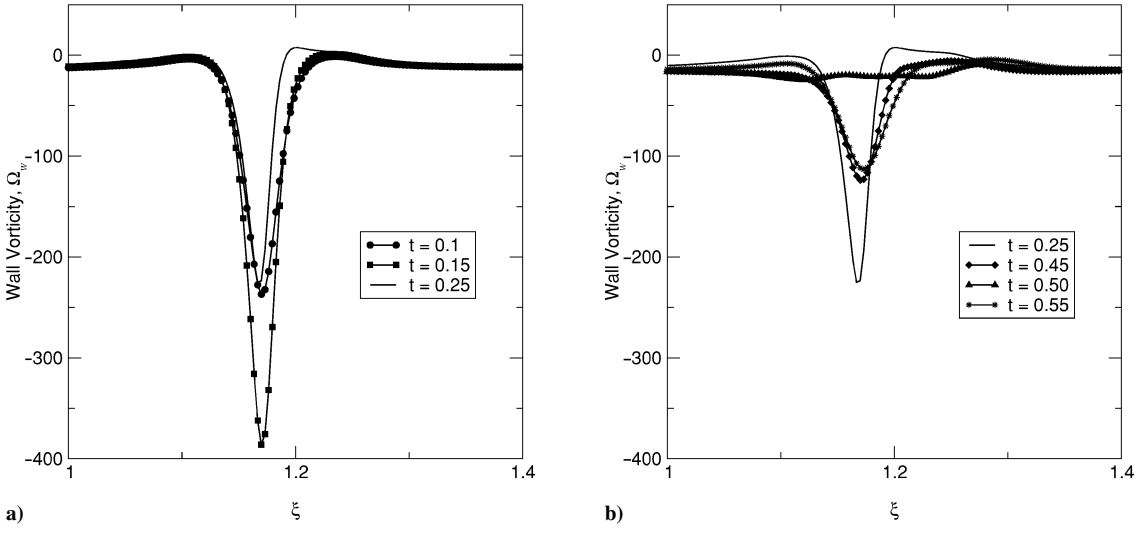

Fig. 7 Wall-vorticity history for a single roughness element showing the a) expansion and b) contraction.

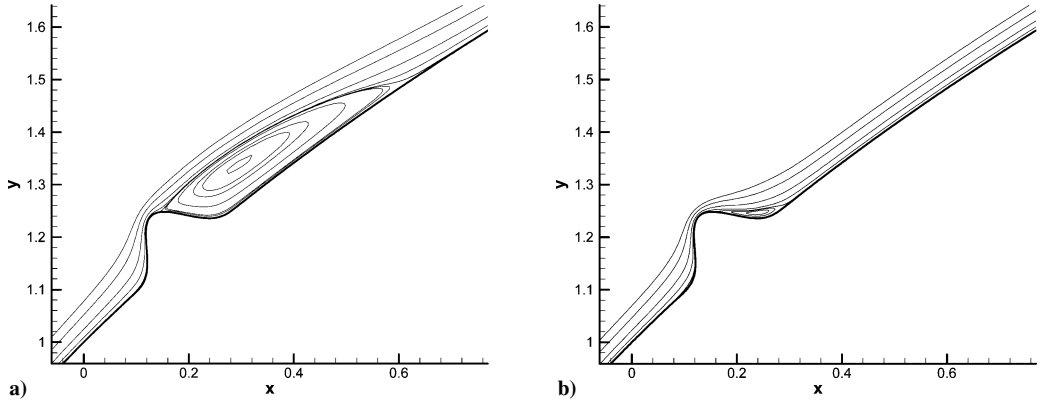

Fig. 8 Flow-field comparison with $Re_l = 1000$ for a) static roughness and b) dynamic roughness.

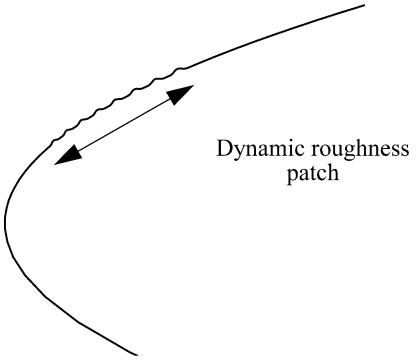

Fig. 9 Typical leading-edge dynamic roughness pattern with roughness fully extended.

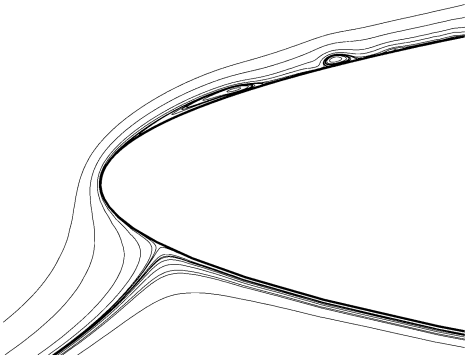

Fig. 10 Stream-function contours for clean airfoil at a static angle-of-attack parameter of $K = 2.0$.

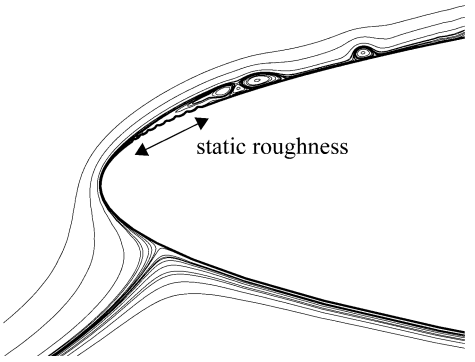

Fig. 11 Stream-function contours for airfoil with static roughness geometry at $K = 2.0$.

A typical dynamic roughness configuration is shown in Fig. 9, which contains eight small humps in the leading-edge region. This figure represents either dynamic roughness in the fully extended scenario or the static roughness. As expected, the full dynamic roughness configuration that can affect flow separation is different for constant angle of attack and for dynamic stall, which includes such things as roughness location and maximum height. It should be noted that for both the constant angle-of-attack and dynamic stall flow separation regimes, effort was made to find a combination of parameters that produced a positive effect on flow separation. However, there has currently been no effort made to optimize these parameters for the given flow condition. It is assumed that each flow condition would have a set of parameters that would yield the optimal flow control conditions. This is deferred for future work.

Three separate cases were investigated that all had the same angle of attack and same freestream Reynolds number: 1) clean airfoil with no roughness, 2) static roughness to match maximum expansion of dynamic roughness, and 3) dynamic roughness. Figure 10 shows the stream function contours for the clean airfoil at $K = 2.0$. This shows an unsteady flow with a leading-edge recirculating region and small vortices being shed downstream.

The static roughness case is shown in Fig. 11. This stream function plot is at the same temporal station as the previous figure. The static roughness clearly shows the formation of a primary vortex and a secondary vortex, along with a shed vortex that is being convected downstream. The flow separation is similar to the clean surface but has more unsteadiness with the surface roughness. The static roughness height is approximately 70% of the oncoming boundary layer height. Folk and Ho[12] point out that the relative size of the perturbation with respect to the boundary-layer height is a key element in the effect a moving boundary has on the flow.

The last case involves the dynamic roughness in place of static roughness. As the dynamic roughness expands in time, the maximum height matches the static roughness height. For this flow separation case, the dynamic roughness produces a significantly different flow pattern at this angle of attack. The primary and secondary vortices formed in the leading-edge region are nonexistent with the dynamic roughness. Only small downstream vortices are seen in the stream function plot of Fig. 12. The dynamic roughness has suppressed the main leading-edge flow separation. It was found during testing that if the maximum dynamic-roughness height exceeded the boundary-layer height, the dynamic motion became detrimental to flow control and the severity of the flow separation increased. Therefore, the size of the perturbations is a crucial element in the application of flow control.

The roughness is located in the vicinity of first separation on the clean surface. Several locations of dynamic roughness were attempted for this flow simulation, which resulted in negligible effects controlling flow separation. Some of the locations and maximum roughness heights produced results similar to the static roughness case. A preliminary conclusion is that each individual flow situation

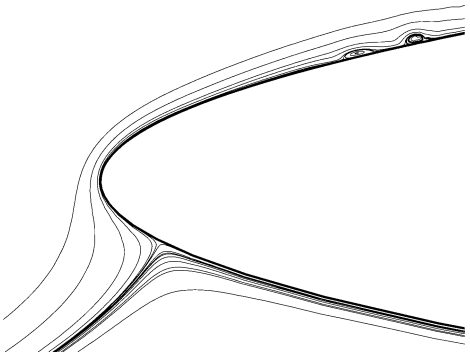

Fig. 12 Stream-function contours for airfoil with dynamic roughness in the leading-edge region at $K = 2.0$ (fully contracted at this physical time stage).

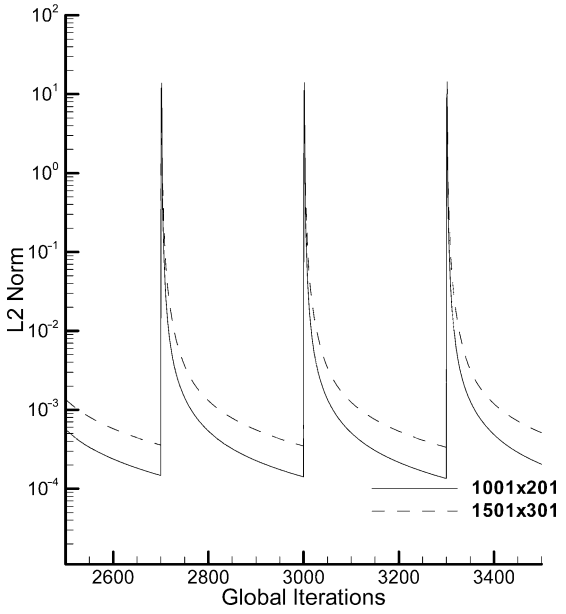

Fig. 13 Global test of the grid convergence for the unsteady flow using the L2 norm values.

will require a slightly different dynamic-roughness configuration. In terms of location, the dynamic roughness will need to be located near the separation point, which is reiterated in Refs. 12 and 19.

It is also assumed that the required frequency of the dynamic roughness will be dependent on the freestream conditions for optimal flow control. The current study only uses one frequency for the dynamic roughness. In terms of a nondimensional number, the Strouhal number for this simulation is approximately 5.2, and is defined as

$$Sr = FA/V_\infty \tag{12}$$

where a standard chord length and flight altitude are used. The dynamic roughness oscillates at a frequency of approximately 60 Hz.

All simulations presented in this study used a grid of 1001×201 with 900 of the streamwise grid points clustered in the patched region of the leading edge. To ensure that there was adequate resolution in the fine-grid patched region, a second grid of 1501×301 (1400 streamwise points in the fine-grid region) was applied to the constant angle-of-attack case with dynamic roughness present on the leading edge. A global comparison was made with the $\Delta\psi$ and $\Delta\Omega$ values at all grid points to generate a plot of the L2 norm for the unsteady flow, shown in Fig. 13. The results for both grids show a decrease in the L2 norm of more than four orders of magnitude. The simulations were allowed 300 iterations in pseudo time before moving to the next physical time step. Refinement of the grid had no effect on the focus area of the dynamic roughness and downstream

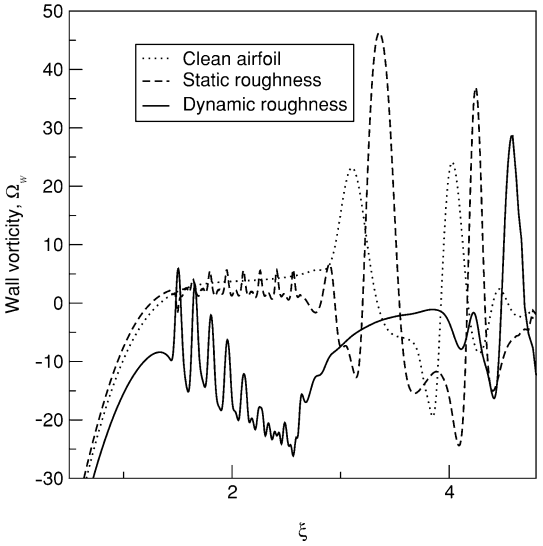

Fig. 14 Wall-vorticity comparison for clean surface, static roughness, and dynamic roughness cases for constant angle of attack.

of this region. The contour plot of stream function for the finer grid compared well with Fig. 12. Therefore, acceptable grid convergence was maintained for the simulations presented in this work. Simulations were also performed to verify that the physical time step was sufficient for the flow physics and that the downstream boundary of the fine-grid patch region was at a sufficient distance as to not affect the upstream flow.

A comparison of the resulting wall vorticity for the three cases is shown in Fig. 14. The plot shows the wall vorticity in the vicinity of the roughness and immediately downstream. In the region of the roughness, the static roughness case shows similar wall vorticity trends as compared to the clean case, other than the local wall oscillations produced by the roughness geometry. Further downstream, both the clean and static roughness cases show large variation in the wall vorticity because of the shed vortices. In contrast, the dynamic roughness case shows a continual decrease in wall vorticity, or increase in negative vorticity, in the region of roughness along with larger local variations. In the localized region, the dynamic roughness adds vorticity to the flow, which can be related to the underlined term in Eq. (9). Just aft of the roughness, the wall vorticity lacks the large variations as seen in the static roughness and clean case; oscillations in the wall vorticity begin further downstream for the dynamic roughness case. Figures 12 and 14 demonstrate that the dynamic roughness can have a significant effect on the flow separation in the leading-edge region. Again, no attempt has been made to optimize the dynamic roughness effects on this particular flow situation.

C. Flow Separation in Dynamic Stall

The second flow separation case investigated was dynamic stall. Here, the airfoil leading edge is pitched up at a rapid rate to promote the formation of the dynamic stall vortex. Huebsch and Rothmayer[15] have shown that dynamic stall is a robust process that is unaltered by small levels of static surface perturbations. Therefore, this was considered a good case to test the effect of the dynamic roughness; if the dynamic roughness can affect this flow phenomenon, then it is likely that it will also affect general unsteady and steady flow separation events.

Three different simulations were performed to examine the effects of dynamic roughness on dynamic stall. The algorithm used to perform the simulations has been thoroughly validated in previous work with and without surface roughness (see Huebsch and Rothmayer[15,22]). The simulations consist of flow past the leading-edge region of a two-dimensional airfoil undergoing a dynamic stall maneuver. For preliminary testing, the chord Reynolds number is set fairly low at 0.7×10^5 for a NACA 0012 airfoil. As with the constant angle-of-attack separation in the previous section, a laborious search

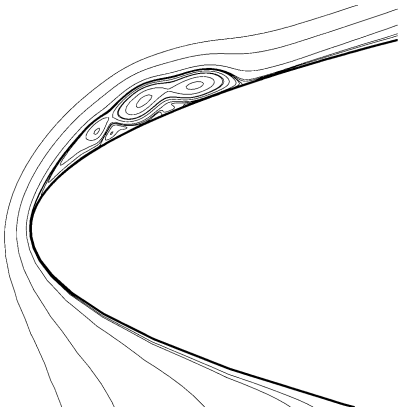

Fig. 15 Stream-function contours of a clean airfoil in dynamic stall at $\tau = 35$.

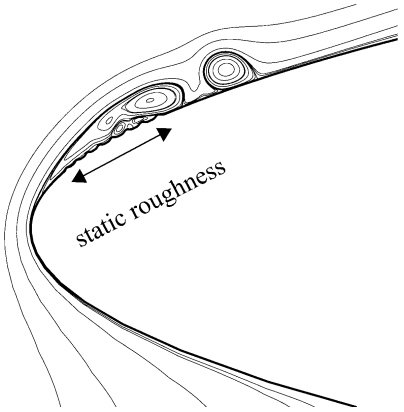

Fig. 16 Stream-function contours for static roughness case in dynamic stall at $\tau = 35$.

through parameter space was required to find a dynamic-roughness configuration that could affect the unsteady separation of dynamic stall. The same basic roughness geometry used for the constant angle of attack was also used here, which is shown in Fig. 9. However, the chord location and maximum roughness height were altered for the dynamic stall case. Most combinations that were attempted had no effect on the formation of the dynamic stall vortex.

Figure 15 shows the clean airfoil undergoing the dynamic stall maneuver at nondimensional physical time of $\tau = 35$. The dynamic stall vortex is fully formed at this point with primary, secondary, and tertiary vortices visible in the leading-edge region. This temporal station of the unsteady vortex formation is just prior to a primary vortex being shed from the surface and convected downstream.

The results of the second simulation are given in Fig. 16, which shows the same airfoil in dynamic stall at the same physical time. However, this case has static surface roughness on the upper leading-edge surface, which is noted in the figure. As can be seen, the formation of the dynamic stall vortex is similar to the clean case, but the static roughness has slightly hastened the process; a primary vortex has already been shed from the surface and is being convected downstream. For much of the rapid pitchup process, the results between clean surface and static-roughness surface were quite similar. At later times, the static surface roughness quickens the unsteady vortex formation.

The final case places the dynamic surface roughness on the leading edge. The roughness parameters were set so that when the dynamic roughness was fully expanded, it was an exact match for the static roughness. For this particular case, shown in Fig. 17, the dynamic roughness was able to suppress the formation of the dynamic stall vortex, which is significant given the fact that the dynamic stall process is fairly robust. The streamlines shown in Fig. 17 are given at the same physical time as the previous figures in the pitchup sequence. The dynamic roughness is in the full contracted position in

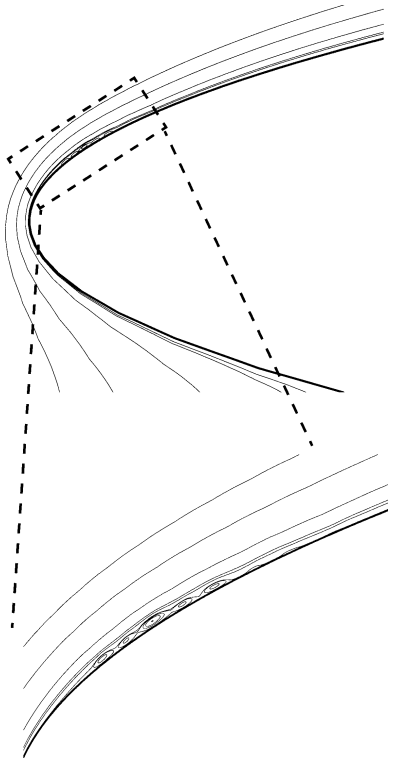

Fig. 17 Stream-function contours for the dynamic roughness case at $\tau = 35$ in dynamic stall, including a close-up of the leading-edge surface region.

this snapshot. If you zoom into the upper surface region where the dynamic roughness is located (also shown in Fig. 17), you can see small unsteady eddies being formed, although they are smaller than the local boundary-layer height. These small eddies were present throughout much of the pitchup sequence but remained localized within the boundary layer. Typically the first phase of the dynamic stall process is the formation of a long separation region on the upper surface of the leading edge. At $\tau = 35$ with the dynamic roughness, this bubble has not yet formed. At $\tau = 39$, the first primary vortex is just starting to form on the leading edge. Therefore, the dynamic roughness has the ability to significantly delay the formation of the dynamic stall vortex and allow the airfoil to reach a higher angle of attack, hence a higher maximum lift coefficient, for the flow conditions tested in this study.

IV. Summary

In this study, a two-dimensional full Navier–Stokes algorithm is used as the basis to develop simulation tools for detailed analysis of moving boundary flow and to investigate the effects of dynamic surface roughness on the flow field. Preliminary computational results reveal that under the currently tested flow conditions, the dynamic roughness can have a major effect on the flow field and the resulting flow is significantly different than the flow field found with a clean airfoil or with similar static surface roughness. The key findings include the following:

1) The Prandtl transposition with body-fitted grids provides an excellent methodology for implementation of moving grids because the surface perturbation and dynamic movement are built into the governing equations.

2) Preliminary results indicate that dynamic roughness can control flow separation and vortex shedding for aerodynamic flows at both constant angle of attack and dynamic stall.

3) It appears that the dynamic injection of vorticity plays a key role in the effects of dynamic roughness on flow separation.

4) Different flow situations will require different dynamic-roughness configurations for the desired effects on flow separation control.

5) The dynamic roughness needs to be placed in the vicinity of the initial separation point.

6) Preliminary indications show that the scale of the dynamic roughness needs to be contained within the boundary layer for the flow-separation cases investigated in this study. Extending the dynamic roughness near or beyond the local boundary-layer height negates the effects of the dynamic perturbations.

As other authors have pointed out, this type of flow control has the potential to be more efficient than the traditional boundary-layer control methods. Given these preliminary results, it seems justified to continue research in this area. Future work should include effects of Reynolds number, maximum roughness height and location, frequency dependence, and dynamic-roughness configurations. These results should then be applied to a three-dimensional study to further investigate the potential of dynamic roughness. Although the simulations and roughness geometries in this study were two dimensional, the stream function–vorticity formulation can be extended to three dimensions by casting the governing equations in a vorticity/stream function–like formulation,[23] which is a subset of the vector potential method. Preliminary work has been done in this area that will lay the groundwork for future research on three-dimensional dynamic roughness simulations.

References

[1]Crank, J., *Free and Moving Boundary Problems*, Oxford Univ. Press, New York, 1984.

[2]Zerroukat, M., and Chatwin, C. R., *Computational Moving Boundary Problems*, Research Studies Press, Somerset, England, 1994.

[3]Shyy, W., Udaykumar, H. S., Rao, M. M., and Smith, R. W., *Computational Fluid Dynamics with Moving Boundaries*, Taylor and Francis, Washington, DC, 1996.

[4]Gad-el-Hak, M., *Flow Control: Passive, Active, and Reactive Flow Management*, Cambridge Univ. Press, New York, 2000.

[5]Pedley, T. J., and Stephanoff, K. D., "Flow Along a Channel with a Time-Dependent Indentation in One Wall: The Generation of Vorticity Waves," *Journal of Fluid Mechanics*, Vol. 160, 1985, pp. 337–367.

[6]Chauve, M. P., and Schiestel, R., "Influence of Weak Wall Undulations on the Structure of Turbulent Pipe Flow: An Experimental and Numerical Study," *Journal of Fluid Mechanics*, Vol. 160, 1985, pp. 47–75.

[7]Lekoudis, S. G., and Sengupta, T. K., "Two-Dimensional Turbulent Boundary Layers over Rigid and Moving Swept Wavy Surfaces," *Physics of Fluids*, Vol. 4, No. 29, April 1986, pp. 965–970.

[8]Bushnell, D. M., Hefner, J. N., and Ash, R. L., "Effect of Compliant Wall Motion on Turbulent Boundary Layers," *Physics of Fluids*, Vol. 20, Pt. 2, Oct. 1977, pp. S31–S48.

[9]Duck, P. W., "Triple-Deck Flow over Unsteady Surface Disturbances: The Three-Dimensional Development of Tollmien–Schlichting Waves," *Computers and Fluids*, Vol. 18, No. 1, 1990, pp. 1–34.

[10]Duck, P. W., "Laminar Flow over Unsteady Humps: The Formation of Waves," *Journal of Fluid Mechanics*, Vol. 160, 1985, pp. 465–498.

[11]Rediniotis, O., Lagoudas, D., Mani, R., Traub, L., Allen, R., and Karniadakis, G., "Computational and Experimental Studies of an Active Skin for Turbulent Drag Reduction," AIAA Paper 2002-2380, July 2002.

[12]Folk, C., and Ho, C. M., "Micro-Actuators for Control of Delta Wing with Sharp Leading Edge," AIAA Paper 2001-0121, Jan. 2001.

[13]Greenblatt, D., and Wygnanski, I. J., "The Control of Flow Separation by Periodic Excitation," *Progress in Aerospace Sciences*, Vol. 36, 2000, pp. 487–545.

[14]White, E. B., and Saric, W. S., "Application of Variable Leading-Edge Roughness for Transition Control on Swept Wings," AIAA Paper 2000-0283, Jan. 2000.

[15]Huebsch, W. W., and Rothmayer, A. P., "The Effects of Surface Ice Roughness on Dynamic Stall," *Journal of Aircraft*, Vol. 39, No. 6, 2002, pp. 945–953.

[16]Werle, M. J., and Davis, R. T., "Incompressible Laminar Boundary Layers on a Parabola at Angle of Attack: A Study of the Separation Point," *Transactions ASME*, Paper 71-APM-31, June 1971.

[17]Reisenthal, P. H., and Childs, R. E., "A Study of Reynolds Number Effects on Incipient Leading Edge Stall," AIAA Paper 94-2339, 1994.

[18]Shyy, W., Pal, S., Udaykumar, H. S., and Choi, D., "Structured Moving Grid and Geometric Conservation Laws for Fluid Flow Computation," *Numerical Heat Transfer, Part A*, Vol. 34, 1998, pp. 369–397.

[19]Gad-el-Hak, M., "Flow Control: The Future," *Journal of Aircraft*, Vol. 38, No. 3, 2001, pp. 402–417.

[20]Van Dyke, M. D., "Second-Order Subsonic Airfoil Theory Including Edge Effects," NASA TR-1274, 1956.

[21]Davis, R. T., "Numerical Solution of the Navier–Stokes Equations for Symmetric Laminar Flow Past a Parabola," *Journal of Fluid Mechanics*, Vol. 51, No. 3, 1972, pp. 417–433.

[22]Huebsch, W. W., and Rothmayer, A. P., "Numerical Prediction of Unsteady Vortex Shedding for Large Leading-Edge Roughness," *Computers and Fluids*, Vol. 33, No. 3, 2004, pp. 405–434.

[23]Matheis, B. D., Rothmayer, A. P., and Huebsch, W. W., "Three-Dimensional Steady Navier–Stokes Calculations of Flow Past Isolated Airfoil Leading Edge Roughness," AIAA Paper 2003-3725, June 2003.